# Variability of the Subantarctic Mode Water volume in the South Indian Ocean during 2004-2018

Yu Hong[1, 2], Yan Du[1, 2, 3*], Tangdong Qu[4], Ying Zhang[1,2], Wenju Cai[5, 6]

[1]State Key Laboratory of Tropical Oceanography, South China Sea Institute of Oceanology, Chinese Academy of Sciences, Guangzhou, China
[2]Southern Marine Science and Engineering Guangdong Laboratory (Guangzhou), Guangzhou, China
[3]University of Chinese Academy of Sciences, Beijing, China
[4]Joint Institute for Regional Earth System Science and Engineering, University of California, Los Angeles, CA, 90095, USA.
[5]Centre for Southern Hemisphere Oceans Research (CSHOR), CSIRO Oceans and Atmosphere, Hobart 7004, Tasmania, Australia
[6]Key Laboratory of Physical Oceanography, Institute for Advanced Ocean Studies, Ocean University of China and Qingdao National Laboratory for Marine Science and Technology, Qingdao, China.

(submitted in 18 NOV 2019, revised in 6 MAR 2020, revised in 17 APR 2020)

*Corresponding author address: Yan Du, State Key Laboratory of Tropical Oceanography, South China Sea Institute of Oceanology, 164 West Xingang Road, Guangzhou 510301, China. E-mail: duyan@scsio.ac.cn

## Key Points:

Argo data reveal a Subantarctic Mode Water volume loss in the South Indian Ocean over the period 2004-2018.

Most of the volume loss occurs in the density range of 26.8-26.9 kg $m^{-3}$, while a volume increase occurs at 26.6-26.8 kg $m^{-3}$.

Changes in the SAMW volume are controlled by surface forcing, which is closely related to the Mascarene High variation.

# Abstract

An analysis of Argo data reveals that the Subantarctic Mode Water (SAMW) in the South Indian Ocean (SIO), characterized by a vertical potential vorticity minimum, decreases by 10% in volume from 2004 to 2015. Most of this decrease occurs at the 26.8-26.9 kg $m^{-3}$density range which forms southwest of Australia, while a slight volume increase occurs at 26.6-26.8 kg $m^{-3}$. Further analysis indicates that the weakening of the Mascarene High and westerly winds in the SIO reduces the evaporation-precipitation, surface heat flux and Ekman pumping and shoals the mixed layer southwest of Australia, which leads to a volume decrease at 26.8-26.9 kg $m^{-3}$ in approximately 3 years. West of 90°E, the parameters exhibit the opposite change, leading to a volume increase at 26.6-26.8 kg $m^{-3}$. This result suggests that surface winds play an important role in the variability of the SIO SAMW volume during the Argo period.



## Plain Language Summary:

During austral winter in the Subantarctic Zone, a water mass called the Subantarctic Mode Water with homogeneous properties (temperature, salinity) forms, sinks, and moves to the interior of the ocean. The formation and transport of the mode water are crucial for the climate, as the water takes up heat, freshwater, carbon, oxygen and nutrients into the ocean interior. We find a distinct volume loss of the mode water in the South Indian Ocean from 2004 to 2018. Although this mode water forms in broad density ranges in different regions, the volume loss only occurs in the dense mode water

south of Australia. Moreover, the volume of the light mode water, which forms in the center of the South Indian Ocean, slightly increases. We find that surface winds control the surface heat flux and water convergence, which determine the volume change here. These winds tend to vary oppositely in the two different mode water formation regions, and make the volume vary in opposition phases. This study reveals the layer dependence of the mode water volume variation and reinforces the importance of atmospheric forcing, which would possibly help interpret the heat uptake in the Southern Ocean.

# 1 Introduction

Mode water refers to a water mass with vertically homogenous physical properties (e.g., temperature and salinity) that covers a large horizontal area of the ocean (Hanawa & Talley, 2001). The Subantarctic Mode Water (SAMW) forms within the Subantarctic Zone (SAZ) during austral winter, when surface cooling leads to deep convection and thus a deep mixed layer (McCartney, 1977). The subducted water then moves northward and westward as part of the southern subtropical gyres at the depth of the main thermocline (McCartney, 1982; Sloyan & Rintoul, 2001; Sallée et al., 2006; Jones et al., 2016), which is believed to play important roles in the heat, freshwater, carbon, oxygen and nutrient budgets both regionally and globally (Sarmiento & Orr, 1991; Sloyan & Rintoul, 2001; Sabine et al., 2004; Sarmiento et al., 2004; Sallée et al., 2013; DeVries et al., 2017).

Due to the spatial and temporal sparsity of observations in the Southern Ocean in the

past, our knowledge of the long-term and large-scale volume variation of the SAMW has been limited. Most earlier studies have focused on the temperature and salinity variations along particular sections and demonstrated substantial oscillations in the SAMW properties (Banks et al. 2000, 2002; Bindoff & McDougall 2002; Bryden et al. 2003). With the increasing coverage of Argo profiles, large-scale examinations of the SAMW thickness have been performed. The results showed a thickening and deepening trend of the SAMW driven by strengthening wind stress curl over the Southern Ocean (e.g., Gao et al., 2018). However, in these studies, the SAMW was defined using a homogeneous temperature in a certain density range without considering differences between ocean basins. In fact, the SAMW is not a uniform water pool (Herraiz-Borreguero & Rintoul , 2011; Jones et al., 2016) and thus exhibits different density ranges in the three ocean basins of the Southern Ocean, where each of these density ranges corresponds to its own formation region and forcing mechanism (Sallée et al., 2006; Herraiz-Borreguero & Rintoul, 2011). Therefore, defining the SAMW using a single homogenous temperature might neglect the dynamic differences between ocean basins. Moreover, Downes et al. (2017) found that the mixed-layer depth (MLD) in the Indian and Pacific Oceans responds differently to wind stress perturbations across SAMW formation zones. They further suggested that the poleward shift of westerly winds rather than an increase in the wind stress curl dominates the SAMW subduction variability in the South Indian Ocean (SIO). In contrast, in the Pacific Ocean, a poleward shift and poleward intensification lead to increases in heat loss and decreases in freshwater input, resulting in a net increase in SAMW subduction.

In the SIO, the SAMW displays a high sensitivity to climate change (Banks et al. 2000). For the first time, this study investigates the layer dependence of the SAMW volume variation in the SIO and its associated atmospheric forcing based on Argo observations. The SAMW here is based on a potential vorticity (PV) minimum definition.

# 2 Data and methods

Temperature and salinity profiling floats (collectively known as Argo floats) have been deployed across the global ocean since 2000, and the number of floats increases with each year. Argo floats monitor the upper ocean up to a depth of 2000 m. These data are of particular importance, especially in the Southern Ocean where long-term observations are sparse. This study utilizes a global data product called the Grid Point Value of the Monthly Objective Analysis (MOAA GPV), which contains monthly temperature and salinity optimally interpolated at the standard pressure levels on a 1° grid based on the observations from Argo floats, the Triangle Trans-Ocean Buoy Network (TRITON), and available conductivity-temperature-depth (CTD) casts (Hosoda, 2007; Hosoda et al., 2008). The MOAA GPV dataset has been employed by many previous studies to investigate the temperature and salinity fields of the ocean (e.g., Kobashi et al., 2019). This dataset spans from 2001 to the present. However, its spatial coverage in the SIO is sparse before 2004 (Figure S1a). Thus, only the data collected during 2004-2018 are used here (Figure S1b).

A thick homogeneous layer forms by deep convection in austral winter, and the homogeneity of this layer can be used to trace the spreading of the SAMW. Another

feature of the SAMW is its low-PV signature, which distinguishes it from the surrounding water. PV, a conservative parameter that provides an excellent tracer for the SAMW (McCartney, 1977, 1982), is given by:

$$PV = \frac{f}{\rho}\frac{d\rho}{dz}$$

where f is the Coriolis parameter, which represents the planetary vorticity, and $\rho = \sigma_0 + 1000$ kg m$^{-3}$ is the potential density referring to the surface. In this study, PV is calculated in the same depth interval as the temperature/salinity. Specifically, the SAMW is defined as a water mass having a PV minimum lower than $0.5\times 10^{-11}$ m$^{-1}$ s$^{-1}$ within the density range of $\sigma_0$=26.6-26.9 kg m$^{-3}$ (Banks et al., 2002; McDonagh et al., 2005; Hasson et al., 2012; Cerovečki et al., 2013).

The MLD is calculated using a density threshold of 0.03 kg m$^{-3}$ from a depth of 10 m, which is suitable for high latitudes in the Southern Hemisphere (de Boyer Montégut et al., 2004; de Lavergne et al., 2014). Furthermore, the heat flux, wind, evaporation (E), and precipitation (P) products from ERA-Interim are used to explain the SAMW volume changes. The net surface buoyancy flux is given by Downes et al. (2010) as follows:

$$B_{net} = \frac{g\alpha}{C_w}H_{in} - g\beta\bar{\rho}S_m(E-P) - B_{Ek}$$

where $H_{in}$ is the net heat flux into the ocean (the sum of shortwave and longwave radiation, and sensible and latent heat fluxes), $g$ is the gravitational constant of acceleration, $\alpha$ is the thermal expansion coefficient, $C_w$ is the heat capacity of seawater, $\beta$ is the haline contraction coefficient, $\bar{\rho}$ is the mean ocean density, $S_m$ is the salinity averaged over the mixed layer, and $E-P$ is the net freshwater flux into

the ocean. The surface buoyancy added by the horizontal Ekman transport (Downes et al., 2010) is given by $B_{Ek} = \frac{g}{\bar{\rho} f} k \times \tau \cdot \nabla \rho_m$, where k is the unit vertical vector, $\rho_m$ is the averaged mixed-layer density and f is the Coriolis parameter. Ekman pumping is estimated as $w_{Ek} = curl[\tau/(\bar{\rho} f)]$. The study region is restricted to 20°E-140°E and 20°S-60°S (Figure S2). Following a previous study (Herraiz-Borreguero & Rintoul, 2011), the upper 100 m is excluded when calculating the SAMW volume to avoid seasonal signals at the top of the water volume.

# 3 SAMW properties

With a detailed inspection of the SAMW properties, this study indicates that there are distinct differences between ocean basins. Figures 1a and c show the PV averaged over 2004-2018 at 32°S, along which a number of repeated hydrographic sections have been conducted (Levitus & Boyer, 1994) and strong regional variations are evident (Sallée et al., 2010). Along this section, the SAMW exists mainly in the Indian and Pacific Oceans, with only a very small amount observed in the Atlantic Ocean (Figure 1a, c). Both the depth and the density ranges of the SAMW are significantly different between the Indian and Pacific Oceans, which is consistent with the findings of a previous study (Herraiz-Borreguero & Rintoul, 2011).

The shallowest and lightest SAMW occurs in the SIO between 60° and 120°E at a depth near 500 m with a density range of $\sigma_0$=26.6-26.9. The SAMW in the Pacific basin appears at ~700 m with a density range of $\sigma_0$=26.9-27.1, which overlaps with the upper portion of the Antarctic Intermediate Water. In each ocean basin, the denser

SAMW is confined to the east, which is consistent with earlier reports that the SAMW density increases from west to east starting at 60°E in the SIO (Hanawa & Talley, 2001; Herraiz-Borreguero & Rintoul, 2011).

The PV distribution along 90°E clearly demonstrates the subduction of the SAMW along isopycnal surfaces in the SIO (Figure 1c). The SAMW forms south of 40°S and extends northward to ~20°S along this section (Figures 1b, d). The thickest SAMW is found at around 35°S, which reflects the influence of horizontal advection in the subtropical gyre. It takes approximately 3 years for the SAMW to reach 30°S after its subduction (Fine et al., 2008; Koch-Larrouy et al., 2010).

The SIO SAMW can be further divided into three major density classes corresponding to different regions of formation (Figure S2): the light SAMW: $26.6<\sigma_0 \leq 26.7$; the medium SAMW: $26.7<\sigma_0 \leq 26.8$; and the dense SAMW: $26.8<\sigma_0 \leq 26.9$. This division is similar to that employed in previous studies (Fine, 1993; Wong, 2005; Koch-Larrouy et al., 2010). The differences in the formation region for the three density classes may imply different forcing mechanisms (Sallée et al., 2006).

# 4 SAMW volume change and spatial distribution

In the SIO, the medium and dense SAMW equally contribute to the total SAMW volume (Figure 2a). During 2004-2018, the total SAMW volume decreases by $0.032 \pm 0.021 \times 10^{15}$ $m^3\,year^{-1}$ (Figure 2a); the uncertainty in this estimate is the 95% confidence interval for the trend. The percentage of this volume decrease ~10% from 2004 to 2018 (Figure 2b). The decrease trend of the SAMW volume in the SIO is

opposite to the thickening trend of the SAMW over the entire Southern Ocean observed in a previous study (Gao et al., 2018). This contrast is likely caused by differences in the definitions employed; that is, Gao et al. defined the SAMW using a density range broader than that used here. As shown in Figure S3a, the water masses at $\sigma_0$=26.5-26.6 and $\sigma_0$=26.5-27.1 increase in volume during the period of observation. Compared with the total volume, the volume of each density class shows a relatively large change. The dense SAMW experiences a decreasing trend of $0.053 \pm 0.027 \times 10^{15}$ m$^3$ year$^{-1}$ from 2004 to 2018, while the medium and light SAMW increase by $0.008 \pm 0.018 \times 10^{15}$ m$^3$ year$^{-1}$ and $0.012 \pm 0.014 \times 10^{15}$ m$^3$ year$^{-1}$, respectively. Note that the medium SAMW trend is small and nonsignificant. The volume trend of the dense and light SAMW is coincident with the two-layer opposite thickness trend for the SIO SAMW over 2006-2015 (Figure 5 in Kolodziejczyk et al., 2019). There appears to be a decadal signal associated with this volume variation (Figures 2a, b), which needs to be confirmed by longer time observations.

Two time periods, 2012-2015 and 2004-2007, are chosen to represent the different states of the SAMW volume, especially for the dense SAMW (Figure 2). The spatial distribution of the SAMW variability in each density class is examined during these two periods. The left panel of Figure 3 shows the low-PV pool along the three isopycnal surfaces. The light SAMW is mainly formed in the central SIO (Figure S2) and extends northwestward to ~30°S (Figure 3a). From the first to the second period, the light SAMW expands, and its thickness increases by more than 50 m (Figure 3b), which contributes to the volume gain. The medium SAMW is mainly formed southwest of

Australia (Figure S2). A dipole pattern is found for both its spatial coverage and its thickness, which decrease in the lower latitudes and increase in the higher latitudes (Figure 3c). This dipole pattern is consistent with the smoothed volume change (Figure 2b). The dense SAMW is mainly formed south of Australia (Figure S2) and extends northwestward to ~20°S in the SIO (Figure 3e). Figure 3e shows that the coverage of the dense SAMW does not change much at higher latitudes; however, the coverage decreases at lower latitudes. This finding implies that the reduction in the dense SAMW volume occurs relatively early. Moreover, the thickness of the dense SAMW decreases by more than 60 m during 2012-2015 (Figure 3f). The decreases in both the spatial coverage and the thickness of the dense SAMW contributes to its volume loss.

# 5 SAMW volume change mechanism

The SAMW forms in the region of deep mixed layer in the SAZ (Figure S2). Changes in the SAMW volume are closely related to the MLD and surface density in austral winter (July, August and September, JAS), as revealed in previous studies (Sallée et al., 2010; Kwon et al., 2013).

The formation of the SAMW is driven by the combined effect of air-sea fluxes and Ekman pumping (McCartney, 1977; Sloyan & Rintoul, 2001; Rintoul & England, 2002; Sloyan et al.,2010; Holte et al., 2012), which in turn are closely related to overlying westerly winds (Downes et al., 2011, 2017).

Most of the decrease in the SAMW spatial coverage occurs at low latitudes (Figure 3e). Since it takes ~3 years for the SAMW to reach 30°S after its subduction (Fine et al.,

2008; Koch-Larrouy et al., 2010), a 3-year time lag is considered to evaluate the MLD change.

The winter MLD in the formation region of the light SAMW at 60°-70°E increases by ~40 m from 2009 to 2012 (Figure 4a), which is consistent with the volume gain with a 3-year lag. Around 120°E, the MLD shows an overall decrease of ~50 m, corresponding to the formation of the dense SAMW; this decrease in the MLD at ~120°E is consistent with the volume loss reflected by the reduced spatial coverage and thickness of the dense SAMW. Generally, the overall decrease in the MLD in the SAMW formation regions from 2009 to 2012 is consistent with the total SAMW volume loss from 2012 to 2015.

A recent study showed that the dynamical process of the increased wind stress curl dominates the thickening of the SAMW (Gao et al., 2018). Here, we clarify the roles of both dynamical and thermal processes in the SIO SAMW volume variation.

The MLD change is driven both by surface buoyancy fluxes, which alter the upper ocean stratification, and by the wind stress curl, which determines the Ekman pumping intensity. Figure 4 shows the thermal and dynamical changes in the surface layer in JAS. The wind pattern change suggests a weak subtropical high during 2009-2012 (Figure 4). Changes in the surface wind induce dipole patterns in the distributions of both E-P and net downward heat flux. West of 90°E, the strengthening of the surface wind enhances evaporation/E-P and heat loss, which induces a net buoyancy loss, resulting in the deepening of the MLD. In contrast, east of 90°E, the weakening of the surface wind reduces evaporation/E-P and heat loss, which induces a net buoyancy gain,

contributing to the shoaling of the MLD (Figures S4a, b). The buoyancy fluxes induced by Ekman transport have positive values in all SAMW formation regions (Figure S4c). The weakening of the westerly wind suppresses the transport of cold and fresh water to the SAMW formation regions, which results in a buoyancy gain. In addition to changes in the surface heat flux and E-P, changes in Ekman heat transport also contribute to the buoyancy gain east of 90°E while partly offsetting the buoyancy loss west of 90°E. Generally, the net surface buoyancy flux around the deep mixed layer shows an increase of ~$2\times 10^{-6}$ kg $m^{-1}$ $s^{-3}$ and a decrease of ~$12\times 10^{-6}$ kg $m^{-1}$ $s^{-3}$ in the regions east and west of 90°E, respectively (Figure 4c). The Ekman pumping change shows a reduction of ~$1\times 10^{-7}$ m $s^{-1}$ east of 90°E, corresponding to a weakened westerly wind, and a slight increase west of 90°E, both of which contribute to the MLD changes in the SAMW formation regions (Figure 4d). To test the sensitivity of this result to the definition of the mixed layer, a temperature threshold of 0.2°C from a depth of 10 m is applied to define the MLD (Dong et al., 2008) and the outcome in Figure S5a reflects essentially the same result.

In general, the dipole patterns of the surface buoyancy flux and Ekman pumping changes are both induced by decadal changes in the subtropical high (Mascarene High, MH; Huang and Tang, 1989) and the associated westerly winds, which dominate the dipole patterns of the MLD and SAMW volume changes in the SIO. Multivariate empirical orthogonal function (MVEOF) analysis (Figure 4e) reveals a dipole pattern similar to those discussed above for changes between the two time periods (Figure 4c). The temporal variation in the JAS MH, defined as the average sea level pressure within

the region of 40°E–105°E, 25°S–35°S (Manatsa et al., 2014), is consistent with the EOF1 time series (Figure 4f). The distinct weakening of the MH during 2000-2018 leads to changes in the SAMW volume with a lag time of ~3 years. The weakening of the MH was similarly mentioned in a recent study (e.g., Vidya et al., 2020). This result implies that the wind anomaly associated with the MH fluctuation plays an important role in generating the surface buoyancy flux, Ekman pumping, and consequently the SAMW volume variability in the SIO.

# 6 Conclusion and discussion

Here, we report the finding of a two-layer density structure with opposite volume trends of the SAMW in the SIO over the last decade. We show that most of the volume decrease occurs at the density range of 26.8-26.9 kg $m^{-3}$, and a slight increase occurs at the range of 26.6-26.7 kg $m^{-3}$. The variation in the SAMW volume is closely connected with a weakening of the subtropical high and associated westerly winds, which intensifies the net buoyancy gain, weakens Ekman pumping, and shoals the deep mixed layer southwest of Australia, leading to a volume decrease at 26.8-26.9 kg $m^{-3}$ that dominates the total SAMW volume in the SIO. Here, we emphasize the importance of a decadal subtropical high variation in the formation of the SAMW in the SIO.

The two-layer density structure of the SAMW with opposite volume trends was recently discussed by two other studies, with one focusing on the entire Southern Ocean and the other focusing on the Pacific Ocean (Portela et al., 2019; Meijers et al., 2019). The former showed that subduction and diapycnal transformation from the lower layer to

the upper layer accounted for most of the upper-layer volume gain and lower-layer volume loss, whereas the latter emphasized the importance of local formation driven by the main atmospheric modes in the Pacific Ocean, which modulate wind stress and turbulent heat fluxes. The results of our study indicate that regional changes in the air-sea heat flux and wind stress associated with the main atmospheric modes have a large impact on the winter MLD and SAMW volume in the SIO. However, the role of diapycnal mixing is not analyzed in this study and needs further investigation.

The increasing ocean heat content (OHC) and deep reaching warming in the Southern Hemisphere have been reported by previous studies (Gao et al., 2018; Volkov et al., 2017). An increasing trend of ~$0.020\pm0.008\times10^{23}$ J $yr^{-1}$ is found for the SIO OHC in the density range of $\sigma_0$=25.6-27.1 (Figure S3b), which is in accordance with the increasing OHC trend of about $0.015\times10^{23}$ J $yr^{-1}$ inferred from a previous study (Llovel & Terray, 2016). We note that this increasing OHC is dominated by an increasing volume of water that is lighter than the SAMW, and thus, the decreasing volume of the dense SAMW partially offsets the increase in the total SIO OHC.

# Acknowledgments:

We acknowledge the Japan Agency for Marine-Earth Science and Technology (JAMSTEC) for providing the Argo temperature and salinity products at http://www.jamstec.go.jp/ARGO/argo_web/argo/?page_id=83&lang=en. We also acknowledge the International Argo Program for collecting these data and making the data freely available (http://www.argo.ucsd.edu, http://argo.jcommops.org). The Argo

Program is part of the Global Ocean Observing System. The wind and surface fluxes are obtained from the ECMWF (https://www.ecmwf.int/). This work is supported by the National Natural Science Foundation of China (41906180, 41525019 and 41830538), the National Basic Research Program of China (2018YFA0605704), the State Oceanic Administration of China (GASI-IPOVAI-02), the Chinese Academy of Sciences (XDA19060501, XDA13010404, ZDRW-XH-2019-2), and the Key Special Project for Introduced Talents Team of the Southern Marine Science and Engineering Guangdong Laboratory (Guangzhou) (GML2019ZD0303, 2019BT2H594). T. Qu was supported by the NSF through grant 1829809. W. Cai is supported by the Centre for Southern Hemisphere Oceans Research, a joint research centre between QNLM and CSIRO, and the Earth Systems and Climate Change Hub of the Australian Government's National Environmental Science Program.

# References:

Argo (2000). Argo float data and metadata from Global Data Assembly Centre (Argo GDAC). SEANOE. http://doi.org/10.17882/42182

Banks, H. T., Wood, R. A., & Gregory, J. M. (2002). Changes to Indian Ocean Subantarctic Mode Water in a Coupled Climate Model as $CO_2$ Forcing Increases. Journal of Physical Oceanography, 32, 2816–2827. doi: 10.1175/1520-0485(2002)032<2816:ctiosm>2.0.co;2

Banks, H. T., Wood, R. A., Gregory, J. M., Johns, T. C., & Jones, G. S. (2000). Are observed decadal changes in intermediate water masses a signature of

anthropogenic climate change? Geophysical Research Letters, 27(18), 2961–2964. doi:10.1029/2000gl011601

Bindoff, N. L., & McDougall, T. J. (2000). Decadal Changes along an Indian Ocean Section at 32°S and Their Interpretation. Journal of Physical Oceanography, 30(6), 1207–1222. doi:10.1175/1520-0485(2000)030<1207:dcaaio>2.0.co;2

Bryden, H. L., McDonagh, E. L., King, B. A. (2003) Changes in Ocean Water Mass Properties : Oscillations or Trends ? Science, 300:2086–2088. doi: 10.1126/science.1083980

Cerovečki, I., Talley, L. D., Mazloff, M. R., & Maze, G. (2013). Subantarctic Mode Water Formation, Destruction, and Export in the Eddy-Permitting Southern Ocean State Estimate. Journal of Physical Oceanography, 43(7), 1485–1511. doi:10.1175/jpo-d-12-0121.1

de Boyer Montégut, C., Madec, G., Fischer, A. S., Lazar, A., & Iudicone, D. (2004). Mixed layer depth over the global ocean: An examination of profile data and a profile-based climatology. Journal of Geophysical Research, 109(C12). doi:10.1029/2004JC002378

de Lavergne, C., Palter, J. B., Galbraith, E. D., Bernardello, R., & Marinov, I. (2014). Cessation of deep convection in the open Southern Ocean under anthropogenic climate change. Nature Climate Change, 4(4), 278–282. doi:10.1038/nclimate2132

DeVries, T., Holzer, M., & Primeau, F. (2017). Recent increase in oceanic carbon uptake driven by weaker upper-ocean overturning. Nature, 542(7640), 215–218.

doi:10.1038/nature21068

Dong, S., Sprintall, J., Gille, S. T., & Talley, L. (2008). Southern Ocean mixed-layer depth from Argo float profiles. Journal of Geophysical Research, 113(C6). doi:10.1029/2006jc004051

Downes, S. M., Bindoff, N. L., & Rintoul, S. R. (2010). Changes in the Subduction of Southern Ocean Water Masses at the End of the Twenty-First Century in Eight IPCC Models. Journal of Climate, 23(24), 6526–6541. doi:10.1175/2010jcli3620.1

Downes, S. M., Budnick, A. S., Sarmiento, J. L., & Farneti, R. (2011). Impacts of wind stress on the Antarctic Circumpolar Current fronts and associated subduction. Geophysical Research Letters, 38 (L11605). doi:10.1029/2011gl047668

Downes, S. M., Langlais, C., Brook, J. P., & Spence, P. (2017). Regional Impacts of the Westerly Winds on Southern Ocean Mode and Intermediate Water Subduction. Journal of Physical Oceanography, 47(10), 2521–2530. doi:10.1175/jpo-d-17-0106.1

Fine, R. A. (1993). Circulation of Antarctic intermediate water in the South Indian Ocean. Deep Sea Research Part I: Oceanographic Research Papers, 40(10), 2021–2042. doi:10.1016/0967-0637(93)90043-3

Fine, R. A., Smethie, W. M., Bullister, J. L., Rhein, M., Min, D. H., Warner, M. J., et al. (2008). Decadal ventilation and mixing of Indian Ocean waters. Deep Sea Research Part I: Oceanographic Research Papers, 55(1), 20–37.

372 doi:10.1016/j.dsr.2007.10.002

373 Gao, L., Rintoul, S. R., & Yu, W. (2017). Recent wind-driven change in Subantarctic
374 Mode Water and its impact on ocean heat storage. Nature Climate Change, 8(1),
375 58–63. doi:10.1038/s41558-017-0022-8

376 Hanawa, K., Talley, L. D. (2001) Mode Waters. In: Ocean Circulation and Climate.
377 Academic Press, pp 373–386

378 Hasson, A., Koch-Larrouy, A., Morrow, R., Juza, M., & Penduff, T. (2011). The
379 origin and fate of mode water in the southern Pacific Ocean. Ocean Dynamics,
380 62(3), 335–354. doi:10.1007/s10236-011-0507-3

381 Herraiz-Borreguero, L., & Rintoul, S. R. (2010). Subantarctic mode water:
382 distribution and circulation. Ocean Dynamics, 61(1), 103–126.
383 doi:10.1007/s10236-010-0352-9

384 Holte, J. W., Talley, L. D., Chereskin, T. K., & Sloyan, B. M. (2012). The role of air-
385 sea fluxes in Subantarctic Mode Water formation. Journal of Geophysical
386 Research: Oceans, 117:1–17. doi:10.1029/2011jc007798

387 Hosoda, S. (2007). Grid Point Value of the Monthly Objective Analysis using the
388 Argo data. JAMSTEC. doi:10.17596/0000102

389 Hosoda, S., Ohira, T., Nakamura, T. (2008). A monthly mean dataset of global
390 oceanic temperature and salinity derived from Argo float observations.
391 JAMSTEC Rep Res Dev 8:47–59. doi: 10.5918/jamstecr.8.47

392 Huang, & Tang (1989). Medium-range oscillation and teleconnection of the
393 atmospheric circulation systems over the Northwest Pacific and South Indian

394 Ocean. Journal of Meteorological Research, 3(5), 571-581.
395 Jones, D. C., Meijers, A. J. S., Shuckburgh, E., Sallée, J.-B., Haynes, P., McAufield,
396 E. K., & Mazloff, M. R. (2016). How does Subantarctic Mode Water ventilate
397 the Southern Hemisphere subtropics? Journal of Geophysical Research: Oceans,
398 121(9), 6558–6582. doi:10.1002/2016jc011680
399 Kobashi, F., Doi, H., & Iwasaka, N. (2019). Sea Surface Cooling Induced by
400 Extratropical Cyclones in the Subtropical North Pacific: Mechanism and
401 Interannual Variability. Journal of Geophysical Research: Oceans, 124(3), 2179–
402 2195. doi:10.1029/2018jc014632
403 Koch-Larrouy, A., Morrow, R., Penduff, T., & Juza, M. (2010). Origin and
404 mechanism of Subantarctic Mode Water formation and transformation in the
405 Southern Indian Ocean. Ocean Dynamics, 60(3), 563–583. doi:10.1007/s10236-
406 010-0276-4
407 Kolodziejczyk, N., Llovel, W., & Portela, E. (2019) Interannual variability of upper
408 ocean water masses as inferred from Argo Array. Journal of Geophysical
409 Research: Oceans, 124(8), 6067-6085. doi: 10.1029/2018JC014866.
410 Kwon, E. Y., Downes, S. M., Sarmiento, J. L., Farneti, R., & Deutsch, C. (2013).
411 Role of the Seasonal Cycle in the Subduction Rates of Upper–Southern Ocean
412 Waters. Journal of Physical Oceanography, 43(6), 1096–1113. doi:10.1175/jpo-
413 d-12-060.1
414 Levitus, S., & Boyer, T. P. (1994). World ocean atlas 1994. volume 4. Temperature
415 Llovel, W., & Terray, L. (2016). Observed southern upper-ocean warming over 2005–

2014 and associated mechanisms. Environmental Research Letters, 11, 124023. doi:10.1088/1748-9326/11/12/124023.

McCartney (1977). Subantarctic mode water. In: Angel M (ed) In avoyage of discovery, supplement to deep–sea research George Deacon 70th anniversary volume. Pergamon, pp 103–119

McCartney (1982). The subtropical recirculation of mode waters. Journal of Marine Research, 40, 427-464

McDonagh, E. L., Bryden, H. L., King, B. A., Sanders, R. J., Cunningham, S. A., & Marsh, R. (2005). Decadal Changes in the South Indian Ocean Thermocline. Journal of Climate, 18(10), 1575–1590. doi:10.1175/JCLI3350.1

Meijers, A. J. S., Cerovečki, I., King, B. A., & Tamsitt, V. (2019). A See-Saw in Pacific Subantarctic Mode Water Formation Driven by Atmospheric Modes. Geophysical Research Letters. doi:10.1029/2019gl085280

Portela, E., Kolodziejczyk, N., Maes, C., & Thierry, V. (2019). Interior water-mass variability in the Southern-Hemisphere oceans during the last decade. Journal of Physical Oceanography. doi:10.1175/jpo-d-19-0128.1

Rintoul, S. R., & England, M. H. (2002). Ekman Transport Dominates Local Air–Sea Fluxes in Driving Variability of Subantarctic Mode Water. Journal of Physical Oceanography, 32(5), 1308–1321. doi:10.1175/1520-0485(2002)032<1308:etdlas>2.0.co;2

Sabine, C. L., Feely, R. A., Gruber, N., Key, R. M., Lee, K., Bullister, J. L., et al. (2004). The oceanic sink for anthropogenic $CO_2$. Science, 305:367–371. doi:

10.1126/science.1097403

Sallée, J. B., Shuckburgh, E., Bruneau, N., Meijers, A. J. S., Bracegirdle, T. J., Wang, Z., & Roy, T. (2013). Assessment of Southern Ocean water mass circulation and characteristics in CMIP5 models: Historical bias and forcing response. Journal of Geophysical Research: Oceans, 118(4), 1830–1844. doi:10.1002/jgrc.20135

Sallée, J. B., Speer, K., Rintoul, S., & Wijffels, S. (2010). Southern Ocean Thermocline Ventilation. Journal of Physical Oceanography, 40(3), 509–529. doi:10.1175/2009jpo4291.1

Sallée, J. B., Wienders, N., Speer, K., & Morrow, R. (2006). Formation of subantarctic mode water in the southeastern Indian Ocean. Ocean Dynamics, 56(5-6), 525–542. doi:10.1007/s10236-005-0054-x

Sarmiento, J. L., Gruber, N., Brzezinski, M. A., & Dunne, J. P. (2011). Erratum: High-latitude controls of thermocline nutrients and low latitude biological productivity. Nature, 479(7374), 556–556. doi:10.1038/nature10605

Sarmiento, J. L., & Orr, J. C. (1991). Three-dimensional simulations of the impact of Southern Ocean nutrient depletion on atmospheric $CO_2$ and ocean chemistry. Limnology and Oceanography, 36(8), 1928–1950. doi:10.4319/lo.1991.36.8.1928

Sloyan, B. M., & Rintoul, S. R. (2001). Circulation, Renewal, and Modification of Antarctic Mode and Intermediate Water. Journal of Physical Oceanography, 31(4), 1005–1030. doi:10.1175/1520-0485(2001)031<1005:cramoa>2.0.co;2

Sloyan, B. M., Talley, L. D., Chereskin, T. K., Fine, R., & Holte, J. (2010). Antarctic

460 Intermediate Water and Subantarctic Mode Water Formation in the Southeast
461 Pacific: The Role of Turbulent Mixing. Journal of Physical Oceanography,
462 40(7), 1558–1574. doi:10.1175/2010jpo4114.1
463 Vidya, P. J., Ravichandran, M., Subeesh, M. P., Chatterjee, S., & Nuncio, M. (2020).
464 Global warming hiatus contributed weakening of the Mascarene High in the
465 Southern Indian Ocean. Scientific Reports, 10(1), 1-9. doi: 10.1038/s41598-020-
466 59964-7
467 Volkov, D. L., Lee, S.-K., Landerer, F. W., & Lumpkin, R. (2017). Decade-long
468 deep-ocean warming detected in the subtropical South Pacific. Geophysical
469 Research Letters, 44(2), 927–936. doi:10.1002/2016gl071661
470 Wong, A. P. S. (2005). Subantarctic Mode Water and Antarctic Intermediate Water in
471 the South Indian Ocean based on profiling float data 2000–2004. Journal of
472 Marine Research, 63(4), 789–812. doi:10.1357/0022240054663196

# Figure Captions:

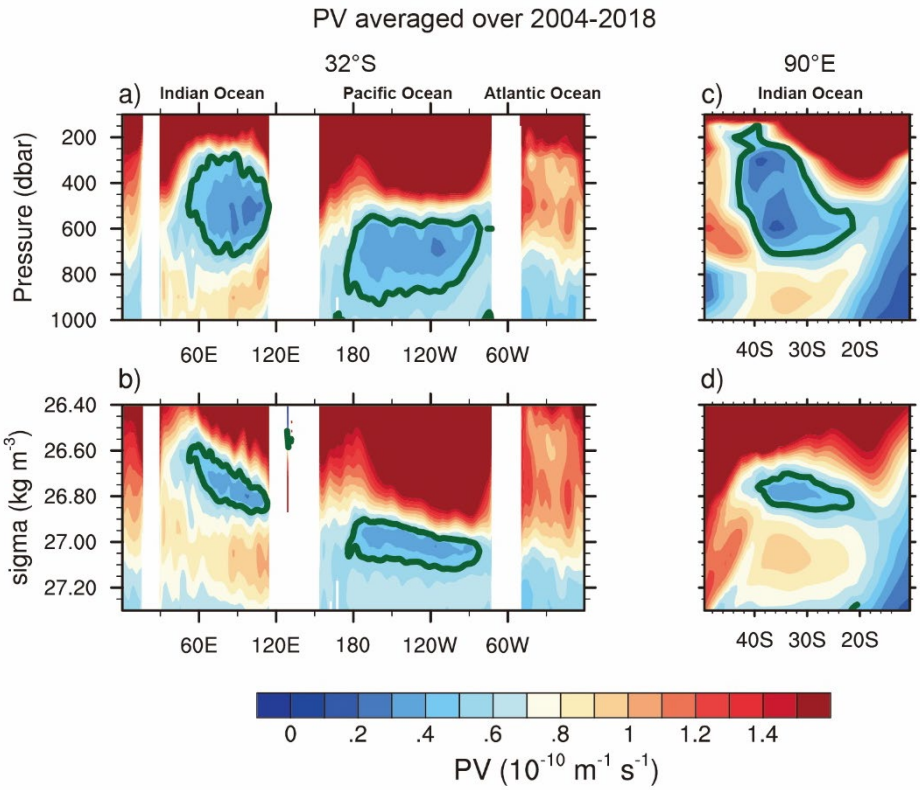


**Figure 1.** PV averaged over the period 2004-2018 in a) pressure and b) sigma coordinates at 32°S and in c) pressure and d) sigma coordinates at 90°E. The green lines indicate the low-PV (lower than $0.5\times10^{-10}$ $m^{-1}$ $s^{-1}$) pool of the SAMW.

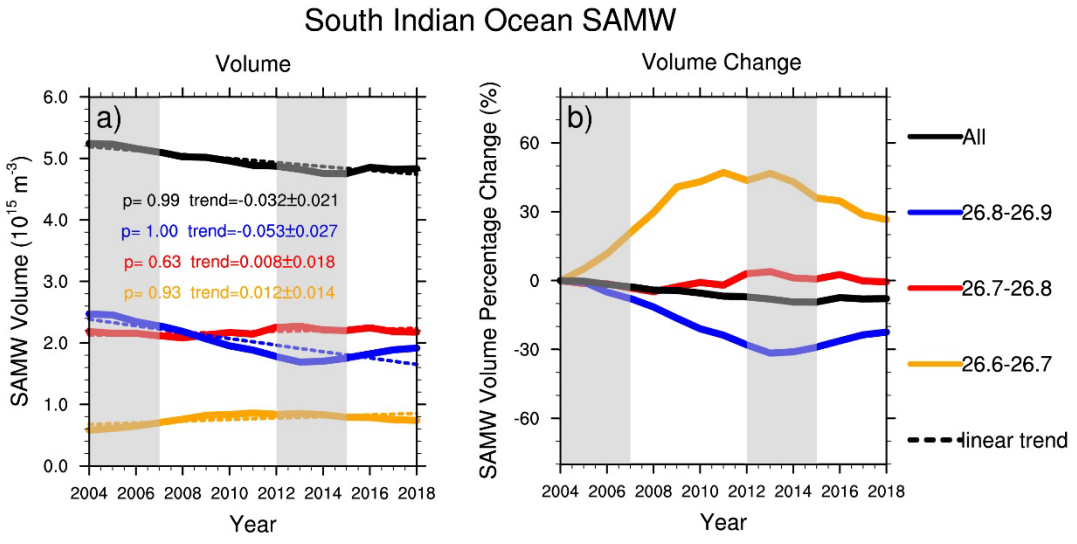


**Figure 2.** Annual mean SAMW in the SIO: a) volume and b) percentage of change

480 relative to 2004 (5-year running average with the first and last two years using their
481 original values). The p-value (for a null hypothesis of zero trend) and the trend with a
482 95% confidence interval are shown in a). The gray shading bar indicates the two
483 different time periods.

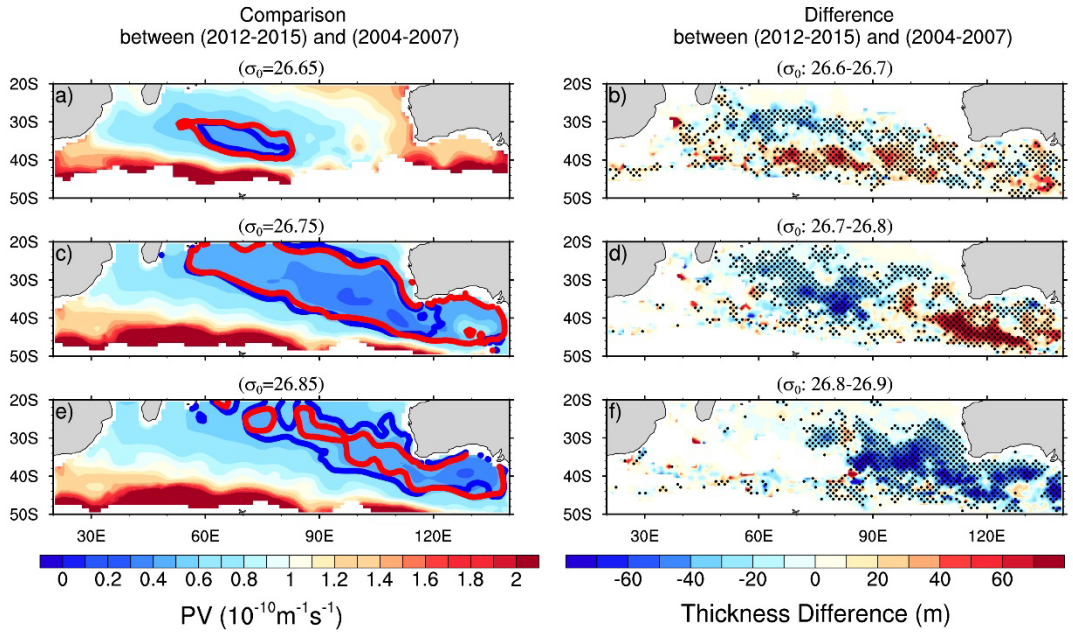


484

485 **Figure 3.** PV averaged over the period 2004-2018 on a) $\sigma_0$=26.65, b) $\sigma_0$=26.75 and c)
486 $\sigma_0$=26.85. The blue and red lines indicate the low-PV (lower than $0.5\times10^{-10}$ $m^{-1}$ $s^{-1}$) pool
487 averaged over 2004-2007 and 2012-2015, respectively. Thickness differences of d)
488 $\sigma_0$=26.6-26.7, e) $\sigma_0$=26.7-26.8 and f) $\sigma_0$=26.8-26.9 between 2012-2015 and 2004-
489 2007 are also included. Stippling indicates values passing the 95% confidence test.

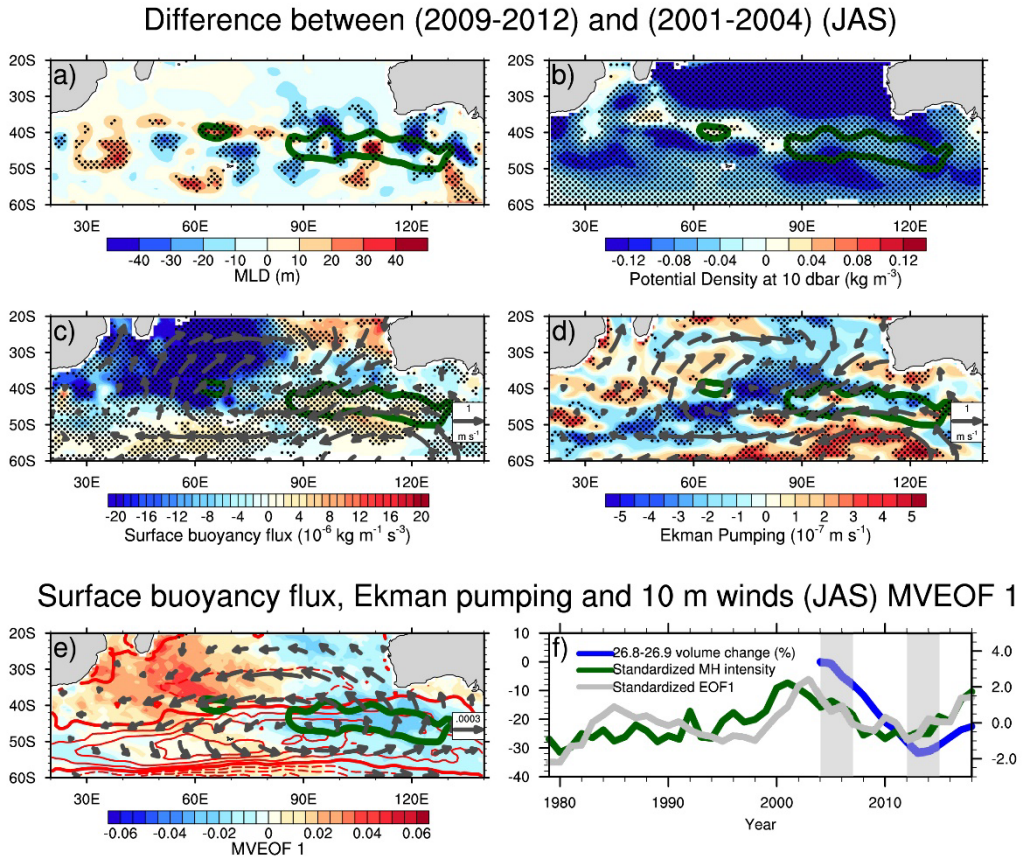


**Figure 4.** Differences between 2009-2012 and 2001-2004 in austral winter (JAS) for the a) MLD, b) potential density at 10 dbar, c) surface buoyancy flux, and d) Ekman pumping. The green lines indicate the region of the deep mixed layer (more than 150 m) where the SAMW forms. The vectors represent the wind differences. MVEOF1 of the surface buoyancy flux, Ekman pumping, and 10 m wind during 1979-2018: e) spatial pattern (colors for the surface buoyancy flux and red lines for Ekman pumping; the bold red line is the zero line) and b) a comparison among the EOF1 time series, MH intensity and $\sigma_0$=26.8-26.9 SAMW volume change (5-year running average with the first and last two years using their original values). Stippling indicates values passing the 95% confidence test.

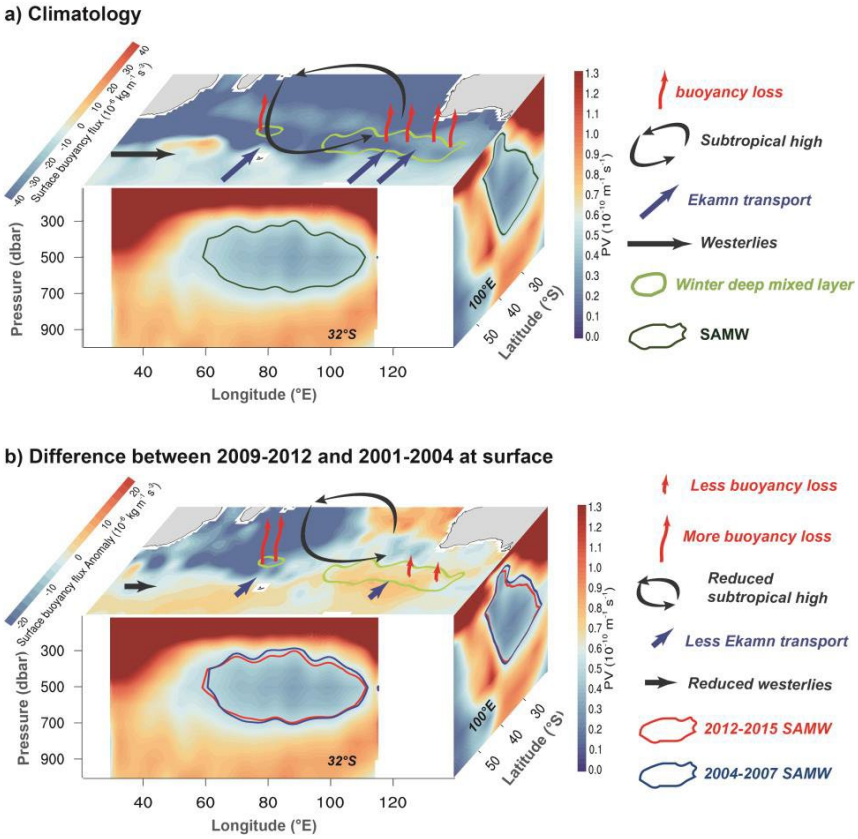


**Figure 5.** Schematic diagram of the main forcing mechanisms for the SIO SAMW formation: a) climatology and b) the difference between 2009-2012 and 2001-2004. The arrows in a) indicate the climatology, and those in b) reflect the final state in 2009-2012.